Supplementary Information for Tunable Interlayer Charge-transfer States in $MoSe_2/WS_2$ Moiré Superlattices

Zheyu Lu[1,2,3,†,*], Jiahui Nie[1,2,3,4,†], Tianle Wang[1,†], Rwik Dutta[5,†], Ruishi Qi[1,3], Jingxu Xie[1,2,3,4], Can Uzundal[1,3,6], Jianghan Xiao[1,2,3], Ziyu Wang[1], Yibo Feng[1], Kenji Watanabe[7], Takashi Taniguchi[8], James R. Chelikowsky[5,9,10], Archana Raja[4,11], Steven G. Louie[1,3], Mit H. Naik[5], Michael P. Zaletel[1], Feng Wang[1,3,11,*]

[1]Department of Physics, University of California at Berkeley, Berkeley, California 94720, USA.
[2]Graduate Group in Applied Science and Technology, University of California at Berkeley, Berkeley, California 94720, USA.
[3]Material Science Division, Lawrence Berkeley National Laboratory, Berkeley, California 94720, USA.
[4]Molecular Foundry, Lawrence Berkeley National Laboratory, Berkeley, California 94720, USA.
[5]Department of Physics, The University of Texas at Austin, Austin, Texas 78712, USA.
[6]Department of Chemistry, University of California at Berkeley, Berkeley, California 94720, USA.
[7]Research Center for Electronic and Optical Materials, National Institute for Materials Science, 1-1 Namiki, Tsukuba 305-0044, Japan.
[8]Research Center for Materials Nanoarchitectonics, National Institute for Materials Science, 1-1 Namiki, Tsukuba 305-0044, Japan.
[9]Center for Computational Materials, Oden Institute for Computational Engineering and Sciences, The University of Texas at Austin, Austin, Texas 78712, USA.
[10]McKetta Department of Chemical Engineering, The University of Texas at Austin, Austin, Texas 78712, USA.
[11]Kavli Energy NanoScience Institute at University of California Berkeley and Lawrence Berkeley National Laboratory, Berkeley, California 94720, USA.

[†]These authors contributed equally.
[*]Correspondence to: zheyulu@berkeley.edu, fengwang76@berkeley.edu

Second harmonic generation

We use second harmonic generation (SHG) to determine the relative alignment of the TMD flakes. The measurements were performed using an amplified femtosecond laser system based on a commercially available Yb:KGW source (Light Conversion, Carbide), which pumps an optical parametric amplifier (OPA, Light Conversion, Orpheus Twins). The idler output of the OPA, tuned to 1060 nm, was focused onto the sample using a 50× microscope objective. The back-reflected SHG signal was collected and imaged onto a cooled camera (Princeton Instruments, PIXIS-100) using a short focal length lens (f = 2.5 cm). The SHG anisotropy was measured by inserting a polarizer and a half-wave plate into the beam path and recording the SHG intensity as a function of the half-wave plate angle.

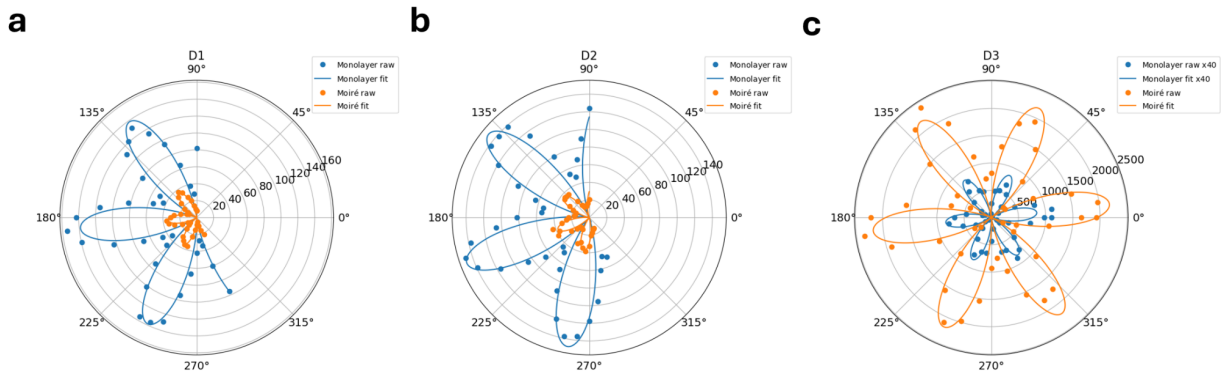

Supplementary Figure 1 | Second harmonic generation (SHG). Polarization-resolved SHG data for the three devices described in this study. In the SHG data, the blue (orange) dots correspond to the integrated SHG signal at different polarization angles θ for the monolayer (moiré) regions, and the solid lines are the corresponding fits to a $\cos^2(3\theta)$ function. **(a)** Device D1: 60°-aligned (H-type) $MoSe_2/WS_2$ heterostructure described in the main text. **(b)** Device D2: 60°-aligned (H-type) $MoSe_2/WS_2$ heterostructure described in the main text. **(c)** Device D3: 0°-aligned (R-type) $MoSe_2/WS_2$ heterostructure described in the main text.

High-energy moiré trion (HET) state

We propose that the HET state is a trion-like state stabilized by moiré localization, derived from the repulsive polaron state of monolayer $MoSe_2$. The monolayer repulsive polaron is known to be a collective bound state from the exciton dressed by the Fermi sea of free electrons, which is gradually blue shifted by the increase in electron density due to Pauli blocking. However, in the moiré heterobilayer, the strong moiré reconstruction of the single-particle bands leads to a great modification of this collective bound state: the repulsive polaron state can be strongly quantized to integer fillings due to the strong interaction with highly localized electrons in each moiré supercell. Specifically, at $n/n_0 = 1$, the c_1 band is half-filled, leading to the Mott-insulating ground state. Each electron can bind with an M_1 exciton, forming an attractive polaron state (LET), leaving the other orthogonal repulsive polaron state to the high-energy side. In the simplest single-particle picture, the HET could be viewed as a bound state composed of a higher-energy exciton and a doped electron at the M site (c_1 band).

Despite its complicated physical origin, the HET state demonstrates a synchronized emergence/annihilation with the LET state and features identical electric field dependence, as shown in Supplementary Figure 2. Both peaks are associated with the doped electron localized at the M site. As a result, these two emergent excitations form a pair of optical probes capable of detecting a single, localized doped electron in the $MoSe_2$ layer.

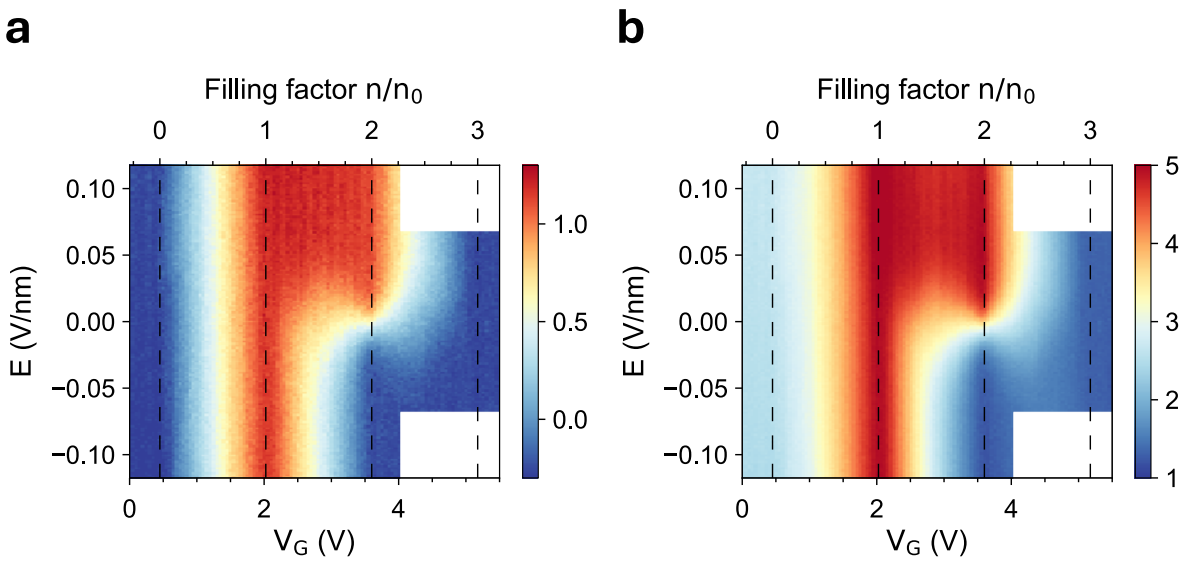

Supplementary Figure 2 | LET vs HET. (a) Peak intensity of the low-energy moiré trion (LET) state in the doping and vertical electric-field two-dimensional parameter space. **(b)** Peak intensity of the high-energy moiré trion (HET) state in the doping and vertical electric-field two-dimensional parameter space.

Additional electron-localization switching behaviors in H-type moiré superlattices

Using the emergent exciton as an optical probe, we extend the study of electron localization to the regime of $n/n_0 = 3$ to 4, where the moiré trion signal is no longer present. The left panel in Supplementary Figure 3a shows the two-dimensional intensity plot of the emergent exciton, which continues to exhibit switching behavior. Supplementary Figure 3b shows the doping-dependent RC spectrum under negative (left) and positive (right) electric fields. Notably, a new lower-energy peak emerges, exhibiting a well-defined magnetic circular dichroism (MCD) signal, as shown in Supplementary Figure 3c. The two-dimensional intensity plot of this new peak is displayed in the right panel of Supplementary Figure 3a. It reveals a complementary pattern to that of the emergent exciton (EX) state. We therefore attribute this new feature to the trion state associated with the EX state, here referred to as the emergent trion (EXT) state, which becomes active when three electrons occupy the M site.

Supplementary Figure 4a shows the two-dimensional map of the EX intensity in device D2, which has a larger electric field range. The blue arrow denotes the electron-localization switching we observed in D1 at $3 < n/n_0 < 4$ (Supplementary Figure 3a). The red arrow, however, denotes a new electron-localization switching at $2 < n/n_0 < 3$ under a large negative electric field. With a large negative electric field, the third doped electron prefers to stay in the $MoSe_2$ layer and fills the c_2 band, which is also localized at the M site. As a result, the EX intensity decreases. It is worth noting that although EX intensity decreases under both large positive and negative electric fields at $2 < n/n_0 < 3$, the underlying electron configuration is totally different for the two switching behaviors.

In summary, we have the following additional electron-localization switching behaviors:

(1) $2 < n/n_0 < 3$: By further increasing the electric field in the negative direction, we can put three electrons at the M site, leading to the potential formation of a quantum many-body complex, such as the Wigner molecule state.

(2) $3 < n/n_0 < 4$: At $n/n_0 = 3$ with a moderate electric field, the energetically stable configuration is two electrons forming a spin-singlet at the M site, and one electron occupying the W site. The additional doped electron can be switched between the W and the M sites by occupying the second moiré conduction band (c_2 band), which is also localized at the M site.

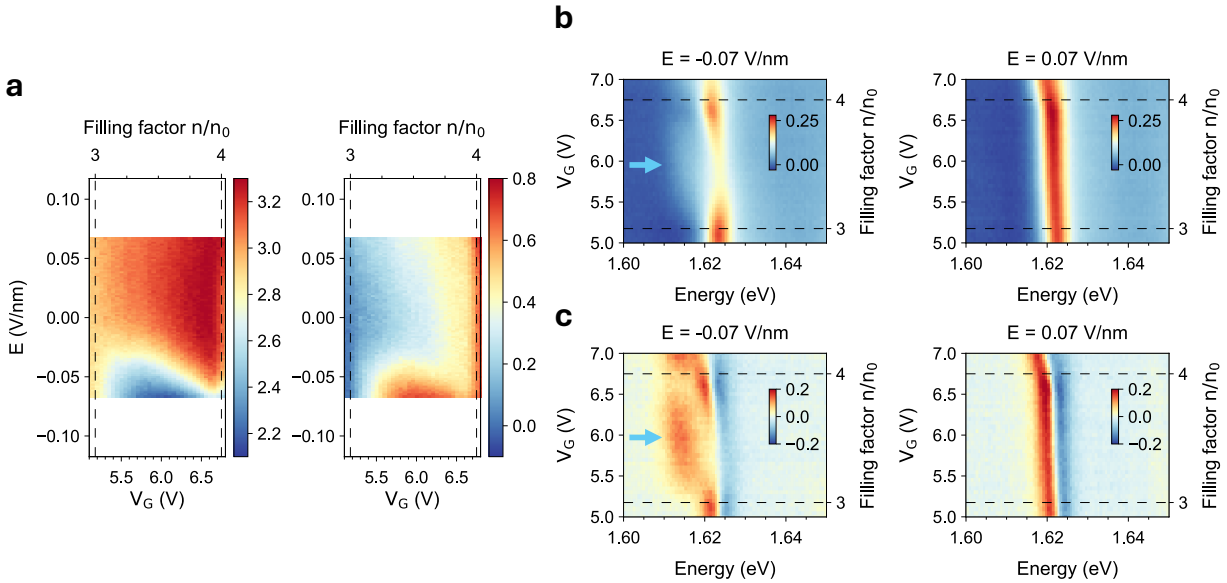

Supplementary Figure 3 | Electron-localization switching at $3 < n/n_0 < 4$ in H-type $MoSe_2/WS_2$ moiré superlattices. (a) Left: Peak intensity of emergent moiré exciton (EX) in the doping and vertical electric field two-dimensional parameter space at $3 < n/n_0 < 4$. Right: Peak intensity of emergent trion (EXT) in the doping and vertical electric field two-dimensional parameter space at $3 < n/n_0 < 4$. **(b)** Experimental reflection contrast spectrum of $MoSe_2/WS_2$ moiré superlattices with electron doping ranging from $n/n_0 = 3$ to 4 under a negative (left) and positive (right) electric field, respectively (zoom-in of Figures 1f and 1g in main text). The blue arrow indicates the EXT state. **(c)** The magnetic circular dichroism (MCD) spectrum corresponding to (b).

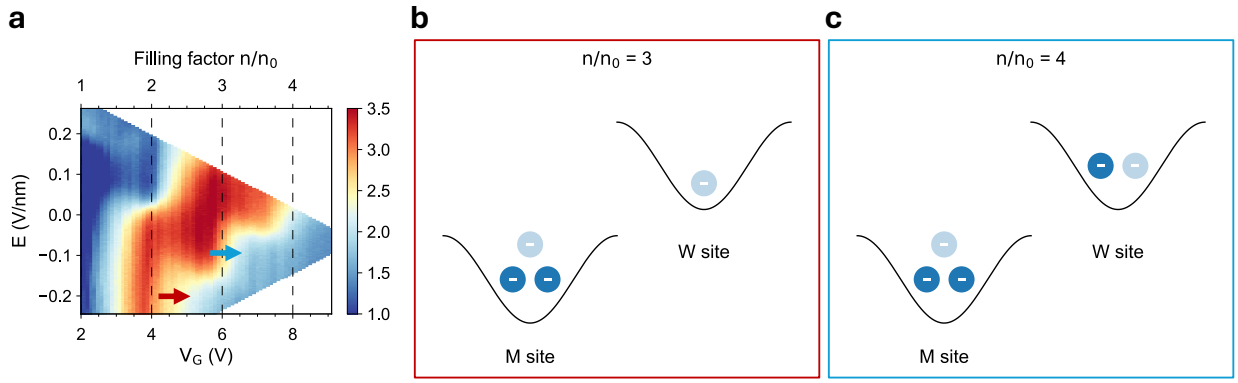

Supplementary Figure 4 | Additional electron-localization switching behaviors in H-type $MoSe_2/WS_2$ moiré superlattices. (a) Peak intensity of emergent moiré exciton (EX) in the doping and vertical electric field two-dimensional parameter space in device D2. The red arrow denotes the additional electron-localization switching behaviors at filling $2 < n/n_0 < 3$ under a large negative electric field, in which case the original three-electron configuration under a moderate electric field is no longer stable. Blue arrow denotes the electron-localization switching behaviors at filling $3 < n/n_0 < 4$, consistent with Supplementary Figure 3a. **(b)** Schematic showing the charge-transfer process indicated by the red arrow in (a). The transparent electron denotes an electric-field-switchable electron. **(c)** Schematic showing the charge-transfer process indicated by the blue arrow in (a). The transparent electron denotes an electric-field-switchable electron.

Electron localization of $n/n_0 = 3$ charge-transfer state in R-type $MoSe_2/WS_2$ moiré superlattices

Here we analyze the possible electron localization for the $n/n_0 = 3$ charge-transfer process in R-type $MoSe_2/WS_2$ moiré superlattices introduced in the main text. The $n/n_0 = 3$ transition appears at $E_{c,3} \approx 0.28$ V/nm. As we show in the main text, at the field below $E_{c,3}$, the $MoSe_2$ side shows a strong EX resonance at $n/n_0 = 3$, while when the field is above $E_{c,3}$, the EX state switches to the LET state. Here, we also include the RC spectrum on the WS_2 side. In Supplementary Figure 5a, the RC spectrum on the WS_2 side shows a well-defined exciton resonance at around 2.02 eV (pointed by the red arrow) and a trion resonance at a lower energy around 2 eV (pointed by the blue arrow). Supplementary Figure 5b further shows the intensity map of the WS_2 trion across the same doping and field range as in the main text (Figure 3d). The WS_2 trion persists for electric fields either below or above $E_{c,3}$, indicating that there is always one electron in the WS_2 layer across the applied electric field range at $n/n_0 = 3$.

Therefore, the $n/n_0 = 3$ charge-transfer process occurs with EX switching to LET on the $MoSe_2$ side, while the WS_2 trion remains unchanged. This scenario gives rise to two possible charge-transfer pathways, as illustrated in Supplementary Figures 5c and 5d. Specifically, one of the two electrons occupying the M site can either transfer to the singly occupied W site or to the unoccupied $B^{Mo/S}$ site (denoted as the W' site).

The first transfer pathway requires a critical electric field $E_{c,3}^{a} \sim (\Delta_0 - U + U_W)/(ed)$, while the second requires $E_{c,3}^{b} \sim (\Delta_1 - U + J_W)/(ed)$. The difference between these critical electric fields is given by $\Delta E_{c,3} = E_{c,3}^{b} - E_{c,3}^{a} \sim (\Delta_1 - \Delta_0) - (U_W - J_W)$, where Δ_0 (Δ_1) denotes the potential energy difference between the $B^{Se/W}$ ($B^{Mo/S}$) stacking, c_{10} (c_{24}) band, in the WS_2 layer and the AA stacking, c_1 band, in the $MoSe_2$ layer. Here, U_W represents the on-site Coulomb

repulsion at the $B^{Se/W}$ stacking site, and J_W denotes the Coulomb interaction between $B^{Se/W}$ and $B^{Mo/S}$ sites in the WS_2 layer.

From DFT calculations, the c_{24} band is approximately 45 meV higher than the c_{10} band, implying $\Delta_1 - \Delta_0 \sim 45$ meV. The critical field required for the $n/n_0 = 2$ charge-transfer process is approximately $\Delta_0 - U_M$. If the second pathway were energetically favored, the additional field required to reach the $n/n_0 = 3$ state would be $(\Delta_1 - \Delta_0) + J_W > 45$ meV. However, experimentally, the increase in electric field from the $n/n_0 = 2$ to the $n/n_0 = 3$ charge-transfer transition is small (less than 0.1 V/nm), corresponding to an energy scale of roughly 25 meV (we use $\epsilon_{hBN}\epsilon_0 E_{hBN} = \epsilon_{TMD}\epsilon_0 E_{TMD}, E_{hBN} \approx (V_T - V_B)/(2d)$, and $\Delta = eE_{TMD}d_{TMD}$, assuming a heterobilayer vertical distance of $d_{TMD} \approx 0.5$ nm and effective out-of-plane dielectric constants $\epsilon_{hBN} = 3.5$ and $\epsilon_{TMD} = 7$). Since this value is significantly smaller than the estimated lower bound, we conclude that the second transfer pathway is energetically unfavorable.

Alternatively, if the first transfer pathway is favored, the required field energies follow the hierarchy: the $n/n_0 = 1$ transition occurs at approximately Δ_0, the $n/n_0 = 2$ transition at $\Delta_0 - U_M$, and the $n/n_0 = 3$ transition lies in between, i.e., $\Delta_0 - U < \Delta_0 - U_M + U_W < \Delta_0$. This implies $U_W < U_M$. Given $\Delta_0 \sim 100$ meV and that the critical field for the $n/n_0 = 2$ transition is about 0.26 V/nm (corresponding to an electron energy of ~ 65 meV), we estimate U_M ~ 35 meV, which leads to $U_W < 35$ meV. Consequently, $U_W - J_W$ must be much smaller than 45 meV (likely in the sub-meV range), yielding $\Delta E_c = E_c^b - E_c^a > 0$, consistent with the first pathway being energetically favored.

We therefore conclude that, for the $n/n_0 = 3$ charge-transfer state, the most likely electron configuration corresponds to the case where one of the two electrons initially occupying the M site

transfers to the singly occupied W site. This results in a singly occupied M site and a doubly occupied W site (Supplementary Figure 5c).

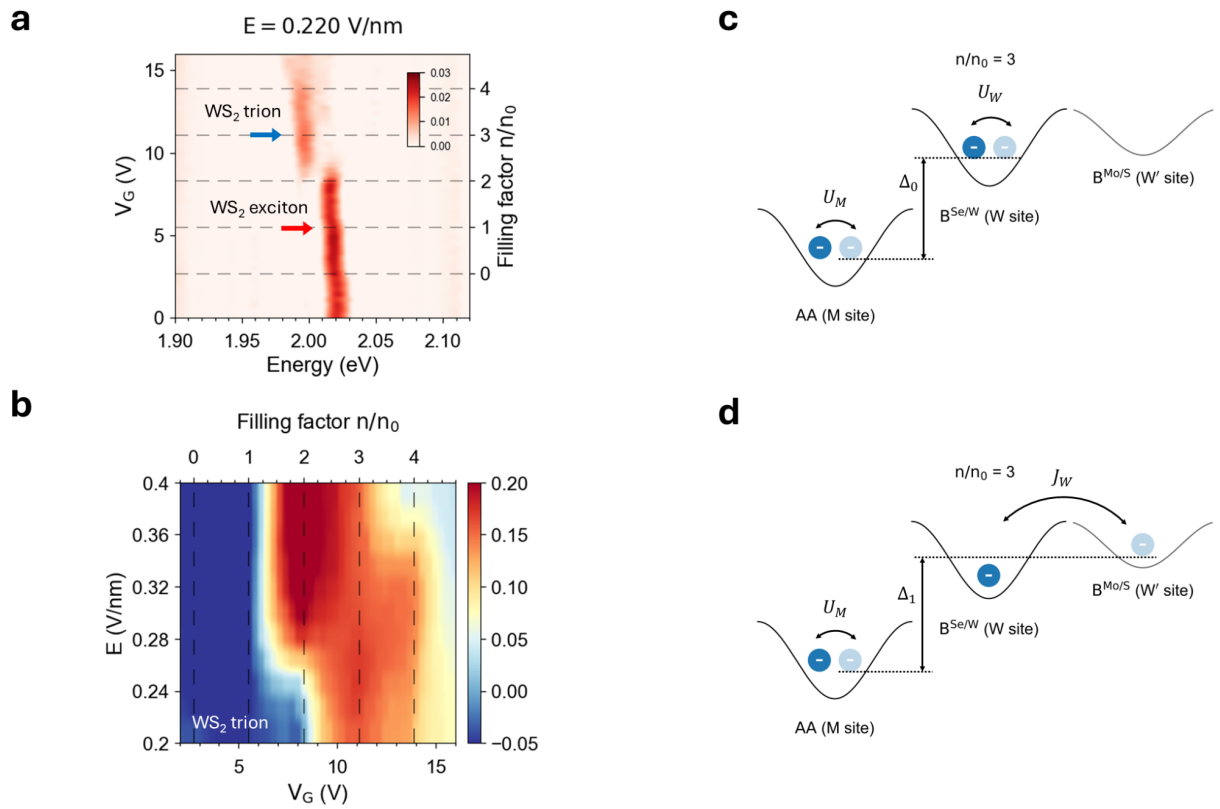

Supplementary Figure 5 | Schematics of two electron-localization configuration candidates for the $n/n_0 = 3$ charge-transfer state in R-type $MoSe_2/WS_2$ moiré superlattices. (a) RC spectrum of the WS_2 layer at $E = 0.22$ V/nm. The blue arrow denotes the moiré trion state of WS_2 at $n/n_0 = 3$. **(b)** Doping-field 2D map of the peak intensity of WS_2 trion state. **(c)** Electrons are switched between the M and the W sites. **(d)** Electrons are switched between the M and the W' site.

Electric field polarization curve in the noninteracting model

In a two-state model without interactions, the LET intensity is given by

$$
\begin{aligned}
I &\propto N - N_1 \\
&= N - N_\mathrm{e} \cdot \frac{\exp\left(-\beta E_1\right)}{\exp\left(-\beta E_1\right) + \exp\left(-\beta E_2\right)} \\
&= N - N_\mathrm{e}/2 + (N_\mathrm{e}/2) \cdot \tanh\left[\beta(ehE - \Delta)/2\right] \\
&\propto (1 - \delta/2) + (\delta/2) \cdot \tanh\left[\beta(ehE - \Delta)/2\right] \\
&= f \cdot \tanh\left[\alpha(E - E_\mathrm{c})\right] + c
\end{aligned}
$$

at filling $1 < \mathrm{n}/\mathrm{n}_0 < 2$, where N is the total number of moiré supercells, N_1 is the number of moiré supercells with two electrons at the M site, N_e is the number of additionally doped electrons from $\mathrm{n}/\mathrm{n}_0 = 1$, $\delta = N_\mathrm{e}/N = \mathrm{n}/\mathrm{n}_0 - 1$ represents the doping level away from $\mathrm{n}/\mathrm{n}_0 = 1$, and $E_{1/2} = E_0 \pm (eEh - \Delta)/2$ denote energies of the M and the W sites at electric field E, respectively. E_0 is the mid-point energy used in the intermediate calculations and does not show up in the final expression. Supplementary Figure 6 shows examples of electric field polarization curves for LET and EX and the corresponding fitting results using the above parametric formula.

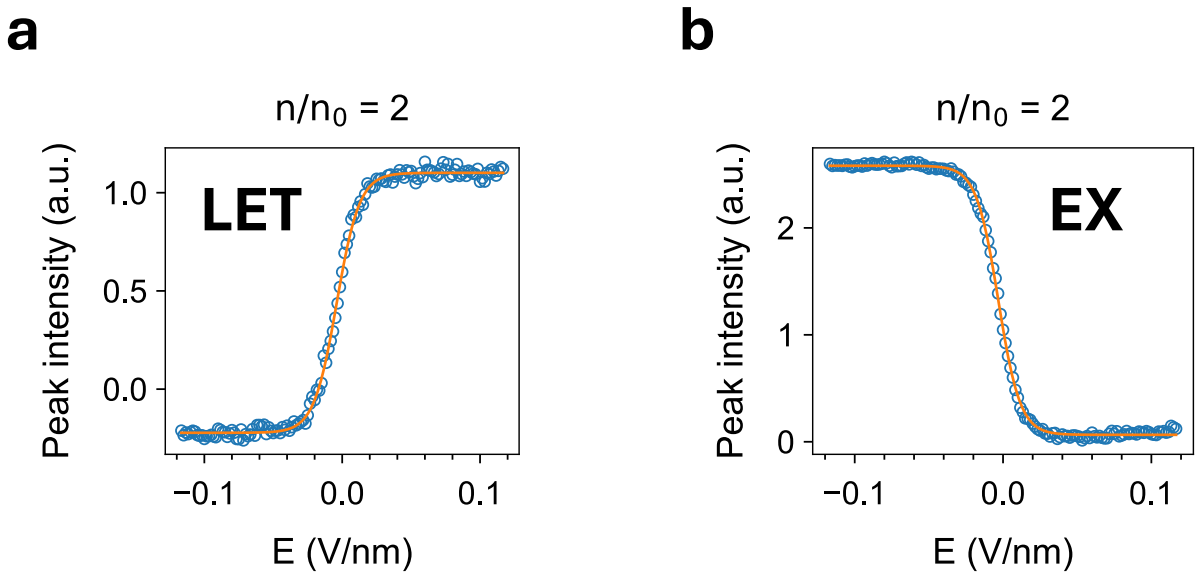

774

775 **Supplementary Figure 6 | Electric field polarization curve in H-type $MoSe_2/WS_2$ moiré**
776 **superlattices. (a)** LET intensity as a function of electric field and its corresponding fitting at n/n_0
777 = 2. **(b)** EX intensity as a function of electric field and its corresponding fitting at $n/n_0 = 2$.

Theoretical calculations

Structural Reconstruction: Aligned bilayer superlattices of $MoSe_2/WS_2$ were constructed at 0° and 60° with the TWISTER code[1]. Experimental lattice constants of 3.28 Å for $MoSe_2$ and 3.15 Å for WS_2 were used. Classical force fields parametrized against van der Waals-corrected density functional theory (DFT) data were employed to relax the moiré superlattices. The Stillinger-Weber[2] and Kolmogorov–Crespi[3,4] potentials were used to describe intralayer and interlayer interactions, respectively, as implemented within the LAMMPS package[5].

Density functional theory: Density functional theory (DFT) calculations[6] of the reconstructed $MoSe_2/WS_2$ moiré superlattice were performed with the SIESTA code[7]. The exchange-correlation effects were treated using generalized gradient approximation following the Perdew-Burke-Ernzerhof (PBE) implementation[8]. Fully relativistic norm-conserving pseudopotentials[9,10] were employed to describe the interactions between valence electrons and ions. The self-consistent ground-state charge density was obtained by γ point sampling of the moiré Brillouin zone. The charge density was then used to construct the DFT Hamiltonian at arbitrary *k*-points across the moiré Brillouin zone, yielding the band structure and wavefunctions needed for subsequent excited-state calculations. Spin-orbit coupling was explicitly included in all calculations.

Pristine unit-cell DFT calculations for the $MoSe_2$ layer were performed using the Quantum Espresso package[11] using identical pseudopotentials and exchange-correlation functional to the SIESTA calculations. The single-particle Kohn-Sham states were expanded in plane waves with a kinetic-energy cutoff of 40 Ry. The Brillouin zone was sampled with a 12×12×1 *k*-point grid to obtain the ground state charge density in an SCF cycle.

GW-BSE: DFT reasonably describes the band dispersions but underestimates the bandgap. To correct the bandgap, we evaluated the quasiparticle energies within the GW self-energy approximation[12] for monolayer $MoSe_2$, as implemented in the BerkeleyGW package[13]. The DFT conduction bands of the reconstructed moiré superlattice were rigidly shifted using the resulting GW correction to the band gap at the K point. The static dielectric function ϵ and screened Coulomb interaction W were evaluated within the random phase approximation, employing a plane-wave energy cutoff of 35 Ry and ~ 5000 unoccupied states. Extension of the dielectric function to finite frequencies was performed using the Hybertsen-Louie generalized plasmon-pole model[12]. The Coulomb potential was truncated in the out-of-plane direction to exclude the spurious effects of periodic images[14]. Convergence of the q-point sampling was enhanced through the nonuniform neck subsampling (NNS) technique[15].

Electron-hole correlations were explicitly treated by the electron-hole interaction kernel in the Bethe–Salpeter equation (BSE)[16]. Brute force computation of the moiré electron-hole kernel is computationally intractable due to the large dimensionality of the moiré electronic wavefunctions. Therefore, the pristine unit-cell matrix projection (PUMP) method[17,18] was employed, which is described in detail below. PUMP is used to construct the moiré superlattice kernel by expressing it as a coherent linear combination of multiple pristine unit-cell kernel matrix elements. The BSE Hamiltonian for the reconstructed $MoSe_2$ superlattice was constructed using 24 valence and 24 conduction bands, with 3×3×1 sampling of the moiré Brillouin zone. These moiré wavefunctions were expanded in terms of 48 valence and conduction states of the pristine superlattice.

Screening was obtained for an AA-stacked $MoSe_2/WS_2$ heterobilayer in the primitive unit-cell to account for the effects of both the layers. The interlayer spacing was chosen to be 6.6 Å which is the average interlayer spacing found in the moiré superlattice. The static dielectric matrix, to compute the unit-cell kernel matrix elements was expanded in plane waves up to 4 Ry and 364 unoccupied states. These pristine unit-cell kernel matrix elements were used to construct the moiré BSE Hamiltonian (more details below) which was diagonalized to obtain the exciton energy levels Ω_S and the exciton envelope function A^S_{cvk}. We then compute the imaginary part of the dielectric function, $\epsilon_2(\omega)$ and the absorption $A(\omega)$ (Supplementary Figure 9). In the weakly absorbing limit, the absorption is expressed as $A(\omega) = \frac{\epsilon_2(\omega)\omega d}{c}$ where d is the sample thickness equal to the average bilayer thickness of 9.8 Å.

Pristine unit-cell matrix projection method: To obtain the moiré excitonic states, we solve the BSE:

$$\left(\mathrm{E}^{\mathrm{QP}}_{\mathbf{ck}} - \mathrm{E}^{\mathrm{QP}}_{\mathbf{vk}}\right)\mathrm{A}^{\mathrm{S}}_{\mathbf{cvk}} + \sum_{v'c'k'} \left\langle \psi^{\mathrm{SL}}_{\mathbf{vk}} \psi^{\mathrm{SL}}_{\mathbf{ck}} \middle| \mathrm{K}^{\mathrm{eh}} \middle| \psi^{\mathrm{SL}}_{v'\boldsymbol{k}'} \psi^{\mathrm{SL}}_{c'\boldsymbol{k}'} \right\rangle \mathrm{A}^{\mathrm{S}}_{c'v'\boldsymbol{k}'} = \Omega_{\mathrm{S}} \mathrm{A}^{\mathrm{S}}_{\mathbf{cvk}}, \qquad (1)$$

where $\mathrm{E}^{\mathrm{QP}}_{\mathbf{nk}}$ denotes the quasiparticle eigenvalues, $\psi^{\mathrm{SL}}_{\mathbf{nk}}$ are the superlattice wavefunctions, $\mathrm{A}^{\mathrm{S}}_{\mathbf{cvk}}$ and Ω_{S} are the exciton eigenfunctions and eigenvalues, respectively. The indices v, c, **k**, correspond to the valence band index, conduction band index, and crystal momentum, respectively. The electron-hole interaction kernel K^{eh} comprises an attractive direct term involving the screened Coulomb interaction and a repulsive exchange term. Evaluation of the kernel matrix elements scales as N^5 with system size, making this a computational bottleneck for large moiré superlattices. The pristine unit-cell matrix projection (PUMP) method reformulates this problem by expressing moiré kernel

as a linear combination of pristine unit-cell kernel matrix elements, yielding a substantial reduction in computational cost.

In the PUMP method, the superlattice electronic wavefunctions are expanded in the basis of primitive unit-cell electronic states. Each valence ($|\psi^{\mathrm{SL}}_{\mathrm{v}\mathbf{k}}\rangle$) and conduction ($|\psi^{\mathrm{SL}}_{\mathrm{c}\mathbf{k}}\rangle$) state in the reconstructed $MoSe_2$ superlattice is expressed as a linear combination of many states of the pristine $MoSe_2$ superlattice: $|\psi^{\mathrm{SL}}_{\mathrm{v}\mathbf{k}}\rangle = \sum_i a_i^{\mathrm{v}\mathbf{k}} |\Phi^{\mathrm{val}}_{i\mathbf{k}}\rangle$, $|\psi^{\mathrm{SL}}_{\mathrm{c}\mathbf{k}}\rangle = \sum_i a_i^{\mathrm{c}\mathbf{k}} |\Phi^{\mathrm{cond}}_{i\mathbf{k}}\rangle$, where $\Phi^{\mathrm{val}}_{i\mathbf{k}}$ and $\Phi^{\mathrm{cond}}_{i\mathbf{k}}$ refer to the pristine superlattice wavefunctions of the valence and conduction states, respectively. The pristine superlattice states are in turn related to states in the primitive unit-cell BZ via band folding. We approximate each electron-hole interaction moiré kernel matrix element, K^{eh}, of the BSE as a coherent sum over many pristine unit-cell kernel matrix elements,

$$\left\langle \psi^{\mathrm{SL}}_{\mathrm{v}\mathbf{k}} \psi^{\mathrm{SL}}_{\mathrm{c}\mathbf{k}} \middle| \mathrm{K}^{\mathrm{eh}} \middle| \psi^{\mathrm{SL}}_{\mathrm{v}'\mathbf{k}'} \psi^{\mathrm{SL}}_{\mathrm{c}'\mathbf{k}'} \right\rangle$$

$$\approx \sum_{ijpq} a_i^{\mathrm{v}\mathbf{k}*} a_j^{\mathrm{c}\mathbf{k}*} a_p^{\mathrm{v}\mathbf{k}} a_q^{\mathrm{c}\mathbf{k}} \left\langle \Phi^{\mathrm{val}}_{i\mathbf{k}_{\mathrm{m}}} \Phi^{\mathrm{cond}}_{j\mathbf{k}_{\mathrm{m}}} \middle| \mathrm{K}^{\mathrm{eh}} \middle| \Phi^{\mathrm{val}}_{p\mathbf{k}'_{\mathrm{m}}} \Phi^{\mathrm{cond}}_{q\mathbf{k}'_{\mathrm{m}}} \right\rangle, \quad (2)$$

$$\approx \sum_{ijpq} a_i^{\mathrm{v}\mathbf{k}*} a_j^{\mathrm{c}\mathbf{k}*} a_p^{\mathrm{v}\mathbf{k}} a_q^{\mathrm{c}\mathbf{k}} \left\langle \phi^{\mathrm{val}}_{s\mathbf{k}^1_{\mathrm{uc}}} \phi^{\mathrm{cond}}_{t\mathbf{k}^2_{\mathrm{uc}}} \middle| \mathrm{K}^{\mathrm{eh}} \middle| \phi^{\mathrm{val}}_{y\mathbf{k}^3_{\mathrm{uc}}} \phi^{\mathrm{cond}}_{z\mathbf{k}^4_{\mathrm{uc}}} \right\rangle, \quad (3)$$

where i and p are pristine valence band indices, j and q are pristine conduction band indices in the superlattice. The pristine states $i\mathbf{k}_{\mathrm{m}}, j\mathbf{k}_{\mathrm{m}}, p\mathbf{k}'_{\mathrm{m}}$ and $q\mathbf{k}'_{\mathrm{m}}$ in the superlattice BZ are related to $s\mathbf{k}^1_{\mathrm{uc}}, t\mathbf{k}^2_{\mathrm{uc}}, y\mathbf{k}^3_{\mathrm{uc}}$ and $z\mathbf{k}^4_{\mathrm{uc}}$ in the unit-cell BZ by band folding, respectively. The kernel in eqn. 2 corresponds to the pristine supercell matrix element, while the kernel matrix elements in eqn. 3 refers to the pristine unit-cell matrix element.

Moiré emergent exciton (EX) state: The EX peak appears in the optical spectrum when two electrons occupy the M site, corresponding to a ground state in which the c_1 band is fully filled. To determine the real-space distribution of this EX state (Supplementary Figure 10), we construct the moiré kernel (eqn. 2) after excluding contributions from the c_1 moiré states. In this procedure, we retain the same screened Coulomb interaction W, neglecting changes in screening corresponding to the removal of the c_1 band.

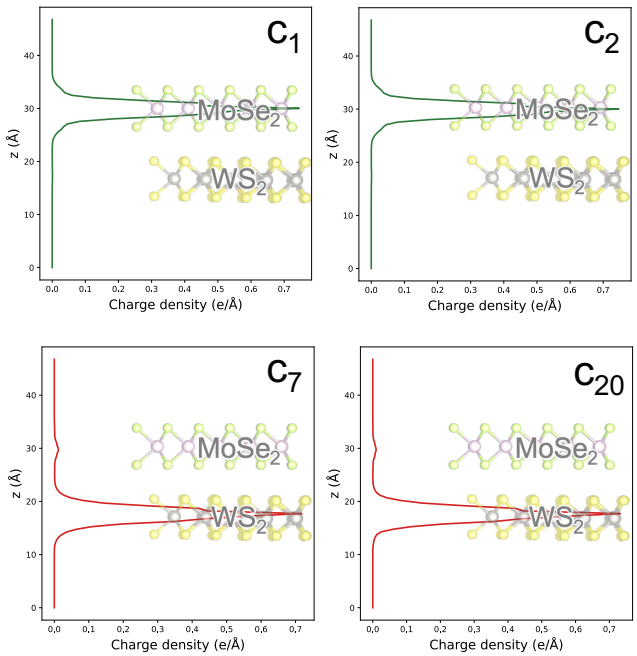

Supplementary Figure 7 | Out-of-plane electron density of H-type $MoSe_2/WS_2$ moiré superlattices. c_1 and c_2 bands are localized in the $MoSe_2$ layer; c_7 and c_{20} bands are the first two lowest energy conduction band states derived from the K valley that are localized in the WS_2 layer.

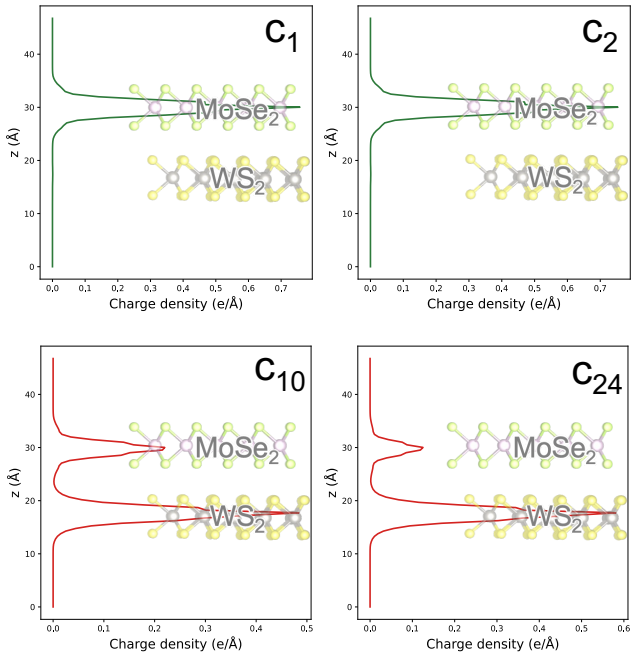

Supplementary Figure 8 | Out-of-plane electron density of R-type $MoSe_2/WS_2$ moiré superlattices. c_1 and c_2 bands are localized in the $MoSe_2$ layer; c_{10} and c_{24} bands are the first two lowest energy conduction band states that are derived from the K valley of the WS_2 layer. We observe some mixing of the c_{10} and c_{24} bands with the $MoSe_2$ states in the R-type configuration.

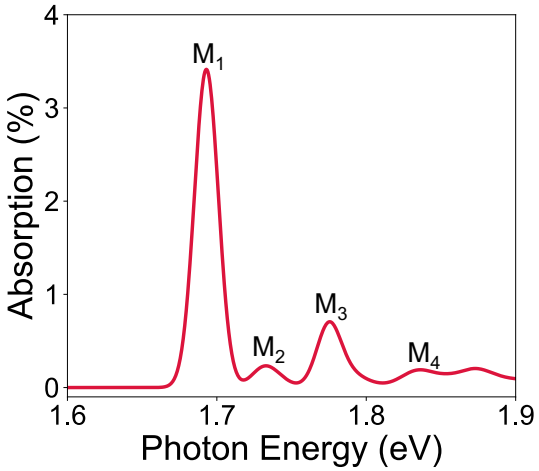

Supplementary Figure 9 | Calculated absorption spectrum. Absorption spectrum of H-type $MoSe_2/WS_2$ moiré superlattices, calculated using first-principles GW-BSE calculations with the PUMP method.

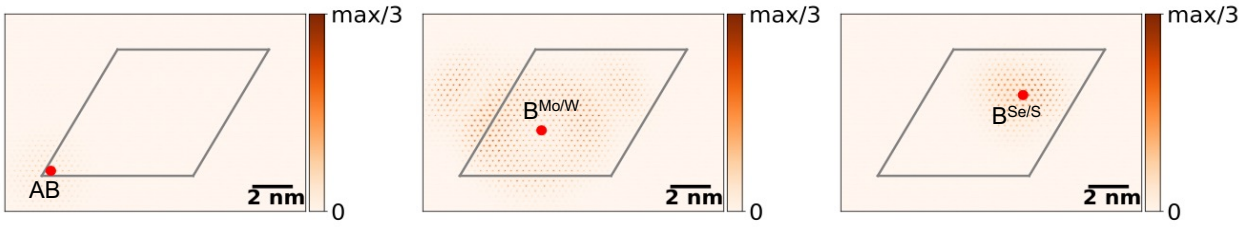

Supplementary Figure 10 | Real-space map of the EX state in H-type $MoSe_2/WS_2$ moiré superlattices. The plot shows the electron density of the exciton, $|\chi(\mathbf{r_e}, \mathbf{r_h})|^2$, for fixed hole positions $\mathbf{r_h}$ (red dot) in the moiré superlattice.

References

1. Saismit Naik *et al.* Twister: Construction and structural relaxation of commensurate moiré superlattices. *Computer Physics Communications* **271**, 108184 (2022).
2. Frank H. Stillinger, and Thomas A. Weber. Computer simulation of local order in condensed phases of silicon. *Physical Review B* **31**, 5262 (1985).
3. Aleksey N. Kolmogorov, and Vincent H. Crespi. Registry-dependent interlayer potential for graphitic systems. *Physical Review B* **71**, 235415 (2005).
4. Mit H. Naik *et al.* Kolmogorov-Crespi potential for multilayer transition-metal dichalcogenides: capturing structural transformations in moiré superlattices. *The Journal of Physical Chemistry C* **123**, 9770-9778 (2019).
5. Aidan P. Thompson *et al.* LAMMPS-a flexible simulation tool for particle-based materials modeling at the atomic, meso, and continuum scales. *Computer Physics Communications* **271**, 108171 (2022).
6. Walter Kohn, and Lu Jeu Sham. Self-consistent equations including exchange and correlation effects. *Physical Review* **140**, A1133 (1965).
7. José M. Soler *et al.* The SIESTA method for ab initio order-N materials simulation. *Journal of Physics: Condensed Matter* **14**, 2745 (2002).
8. John P. Perdew, Kieron Burke, and Matthias Ernzerhof. Generalized gradient approximation made simple. *Physical Review Letters* **77**, 3865 (1996).
9. D. R. Hamann. Optimized norm-conserving Vanderbilt pseudopotentials. *Physical Review B* **88**, 085117 (2013).
10. Michiel J. Van Setten *et al.* The PseudoDojo: Training and grading a 85 element optimized norm-conserving pseudopotential table. *Computer Physics Communications* **226**, 39-54 (2018).
11. Paolo Giannozzi *et al.* QUANTUM ESPRESSO: a modular and open-source software project for quantum simulations of materials. *Journal of Physics: Condensed Matter* **21**, 395502 (2009).
12. Mark S. Hybertsen, and Steven G. Louie. Electron correlation in semiconductors and insulators: Band gaps and quasiparticle energies. *Physical Review B* **34**, 5390 (1986).
13. Jack Deslippe *et al.* BerkeleyGW: A massively parallel computer package for the calculation of the quasiparticle and optical properties of materials and nanostructures. *Computer Physics Communications* **183**, 1269-1289 (2012).
14. Sohrab Ismail-Beigi. Truncation of periodic image interactions for confined systems. *Physical Review B* **73**, 233103 (2006).
15. Felipe H. da Jornada, Diana Y. Qiu, and Steven G. Louie. Nonuniform sampling schemes of the Brillouin zone for many-electron perturbation-theory calculations in reduced dimensionality. *Physical Review B* **95**, 035109 (2017).
16. Michael Rohlfing, and Steven G. Louie. Electron-hole excitations and optical spectra from first principles. *Physical Review B* **62**, 4927 (2000).

17. Mit H. Naik *et al.* Intralayer charge-transfer moiré excitons in van der Waals superlattices. *Nature* **609**, 52-57 (2022).
18. Hongyuan Li *et al.* Imaging moiré excited states with photocurrent tunnelling microscopy. *Nature Materials* **23**, 633-638 (2024).